Flow and stress induced cavitation in a journal bearing with axial throughput

A. Pereira[1†], G. McGrath[2] and D.D. Joseph[1]

[1]University of Minnesota, Minneapolis MN 55454
[2] PDVSA Intevep S.A., Venezuela
[†] Mailing address c/o PDVSA Intevep

September 2000

Abstract

The problem of predicting flow between rotating eccentric cylinders with axial throughput is studied. The system models a device used to test the stability of emulsions against changes in drop size distribution. The analysis looks for the major variation in flow properties which could put an emulsion at risk due to coalescence or breakage and finds the most likely candidate in the pressure gradient defined as the ratio of the difference between the maximum and minimum pressure to the arc length between the difference. The axial throughput is modeled by flow driven by a constant pressure gradient. The flow is calculated from the Navier-Stokes equation using the code SIMPLER (Patankar [1]). The effects of inertia at values typical for the device are studied. Several eccentricities and different rotational speeds are computed to sample the changes in flow and stress parameters in the idealized device for typical conditions. The numerical analysis is validated against the lubrication approximation in the low Reynolds number case. Conditions for stress induced cavitation are evaluated.

The flow is completely determined by a Reynolds number, an eccentricity ratio and a dimensionless pressure gradient and all computed results are either presented or can be easily expressed in terms of these dimensionless parameters.

The effect of inertia is to shift the eddy or re-circulation zone which develops in the more open region of the gap toward the region of low relative pressure; the zero of the relative pressure migrates away from the center and the distribution breaks the skew symmetry of the Stokes flow solution.

The state of stress in the journal bearing is analyzed and a cavitation criterion based on the maximum tensile stress is compared with the traditional criterion based on pressure.

1 Introduction

A diagram of the device we wish to model is shown in figure 1. The model is an idealized version of the device, which can be described as infinitely long rotating eccentric cylinders with a throughput maintained by a constant pressure gradient. The device is used to study the stability of emulsions against changes in the distribution of the drop sizes by *putting the emulsion at great risk* as it passes through the narrow gap. The emulsion is put into a high pressure gradient as it is drawn by shear through the converging high pressure to the diverging low pressure sections. It is probable that the crowded emulsion acts like moving fixed bed, with the more mobile water driven through permeable bed of oil droplets. Our model goes only part of the way in the analysis of emulsion quality meter (EQM, US patent 5,987,969 Nov 23, 1999 Joseph [2]) since the effect of the particles is not considered and the geometry of the device is severely simplified.

There is much literature on the flow between eccentric rotating cylinders. To our knowledge no analysis of the flow between eccentric rotating cylinders with throughput has appeared in the literature. The analysis of stress induced cavitation given here is the first in the lubrication literature and applies ideas formulated by Joseph [3] to a concrete situation.

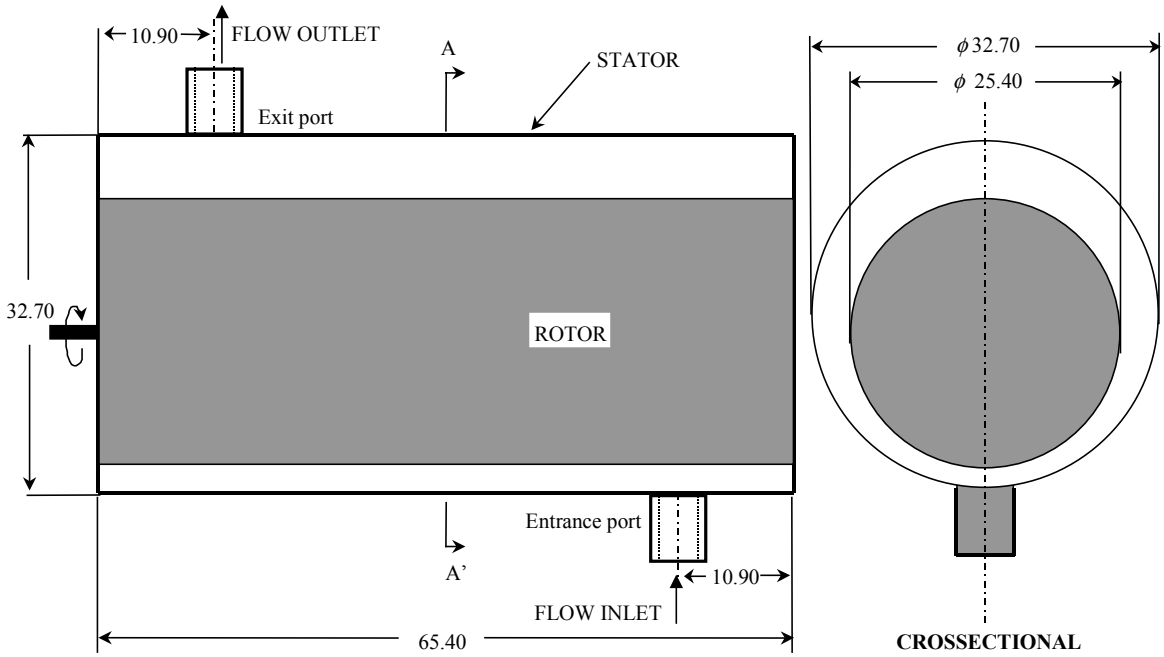

Notes:
1- All the measurements are in mm.
2- The rotor-stator array indicated in this plot was chosen at random

Figure 1. Diagram of the emulsion quality meter (EQM, patent 5,987,969 Nov 23, 1999 Joseph [2]). A highly concentrated oil in water emulsion is forced under pressure from the inlet to the outlet as the rotor turns at a rapid rate. The residence time is controlled by the pressure between the ports and the emulsion is milled as it passes through the minimum gap many times. The milling is controlled by the fluid flow. The pressure between the ports is idealized with a constant pressure.

2 Governing equations

We assume that the axial flow is fully developed, so that the pressure is a linear function of the axial coordinate z; all other quantities are independent of z. The equations of motion are written in cylindrical coordinates with r, θ, z components of velocity $v(r,\theta)$, $u(r,\theta)$ w (r,θ) and relative pressure $p(r,\theta)$ satisfying

$$\frac{1}{r}\frac{\partial}{\partial r}(rv)+\frac{1}{r}\frac{\partial u}{\partial \theta}=0, \tag{1}$$

$$\rho\left(v\frac{\partial v}{\partial r}+\frac{u}{r}\frac{\partial v}{\partial \theta}-\frac{u^2}{r}\right)=-\frac{\partial p}{\partial r}+\mu\left[\frac{\partial}{\partial r}\left(\frac{1}{r}\frac{\partial}{\partial r}(rv)\right)+\frac{1}{r^2}\frac{\partial^2 v}{\partial \theta^2}-\frac{2}{r^2}\frac{\partial u}{\partial \theta}\right], \tag{2}$$

$$\rho\left(v\frac{\partial u}{\partial r}+\frac{u}{r}\frac{\partial u}{\partial \theta}+\frac{vu}{r}\right)=-\frac{1}{r}\frac{\partial p}{\partial \theta}+\mu\left[\frac{\partial}{\partial r}\left(\frac{1}{r}\frac{\partial}{\partial r}(ru)\right)+\frac{1}{r^2}\frac{\partial^2 u}{\partial \theta^2}+\frac{2}{r^2}\frac{\partial v}{\partial \theta}\right], \tag{3}$$

$$\rho\left(v\frac{\partial w}{\partial r}+\frac{u}{r}\frac{\partial w}{\partial \theta}\right)=-\Re+\mu\left[\frac{1}{r}\frac{\partial}{\partial r}\left(r\frac{\partial w}{\partial r}\right)+\frac{1}{r^2}\frac{\partial^2 w}{\partial \theta^2}\right], \tag{4}$$

where $\Re$ is the constant pressure gradient and

$$p(r,\theta)=p_{abs}(r,\theta,z)-p_r(z), \tag{5}$$

is the difference between the absolute pressure p_{abs} and the reference pressure

$$p_r(z)=p_r(0)+\Re z. \tag{6}$$

When the fluid is at rest

$$p_{abs}=p_r(0) \tag{7}$$

The boundary conditions are

$$\left.\begin{array}{l} v,u,w,p \text{ are periodic in } \theta \text{ with period } 2\pi, \\ v,w \text{ vanish on the rotor and stator,} \end{array}\right\} \tag{8}$$

$$u(a,\theta)=U \text{ independent of } \theta \text{ on the rotor } r=a. \tag{9}$$

When the cylinders are concentric, the outer cylinder is at $r = b$ and the clearance is

$$c=b-a. \tag{10}$$

The equation defining of the stator surface is

$$r = \Delta(\theta) = \left[b^2 - (e\sin\theta)^2\right]^{1/2} - e\cos\theta \tag{11}$$

where $\delta = \Delta(0)$ is the minimum gap. The eccentricity is given by

$$e = c - \delta \tag{12}$$

The outer boundary is the average radius of the stator

$$b = \frac{1}{2\pi}\int_0^{2\pi} \Delta(\theta)\,\mathrm{d}\theta\,. \tag{13}$$

Equations (1), (2) and (3) can be solved for u (r,θ), $v(r,\theta)$ and $p(r,\theta)$; then (4) can be solved for w.

3 Dimensionless equations

Dimensionless forms of the equations can be formed using c as the unit of length and U as the unit of velocity. The dimensionless variables are

$$\left(\tilde{r},\theta,\tilde{v},\tilde{u},\tilde{w},\tilde{p},\tilde{e},\tilde{\delta},\tilde{\Re}\right) = \left(\frac{r}{c},\theta,\frac{v}{U},\frac{u}{U},\frac{w}{U},\frac{p}{\rho U^2},\frac{e}{c},\frac{\delta}{c},,\frac{\Re c}{\rho U^2}\right) \quad \frac{1}{\tilde{r}}\frac{\partial}{\partial\tilde{r}}(\tilde{r}\tilde{v}) + \frac{1}{\tilde{r}}\frac{\partial\tilde{u}}{\partial\theta} = 0 \tag{14}$$

$$\tilde{v}\frac{\partial\tilde{v}}{\partial\tilde{r}} + \frac{\tilde{u}}{\tilde{r}}\frac{\partial\tilde{v}}{\partial\theta} - \frac{\tilde{u}^2}{\tilde{r}} = -\frac{\partial\tilde{p}}{\partial\tilde{r}} + \frac{1}{\mathrm{Re}}\left[\frac{\partial}{\partial\tilde{r}}\left(\frac{1}{\tilde{r}}\frac{\partial}{\partial\tilde{r}}(\tilde{r}\tilde{v})\right) + \frac{1}{\tilde{r}^2}\frac{\partial^2\tilde{v}}{\partial\theta^2} - \frac{2}{\tilde{r}^2}\frac{\partial\tilde{u}}{\partial\theta}\right], \tag{15}$$

$$\tilde{v}\frac{\partial\tilde{u}}{\partial\tilde{r}} + \frac{\tilde{u}}{\tilde{r}}\frac{\partial\tilde{u}}{\partial\theta} + \frac{\tilde{v}\tilde{u}}{\tilde{r}} = -\frac{1}{\tilde{r}}\frac{\partial\tilde{p}}{\partial\theta} + \frac{1}{\mathrm{Re}}\left[\frac{\partial}{\partial\tilde{r}}\left(\frac{1}{\tilde{r}}\frac{\partial}{\partial\tilde{r}}(\tilde{r}\tilde{u})\right) + \frac{1}{\tilde{r}^2}\frac{\partial^2\tilde{u}}{\partial\theta^2} + \frac{2}{\tilde{r}^2}\frac{\partial\tilde{v}}{\partial\theta}\right], \tag{16}$$

$$\tilde{v}\frac{\partial\tilde{w}}{\partial\tilde{r}} + \frac{\tilde{u}}{\tilde{r}}\frac{\partial\tilde{w}}{\partial\theta} = -\tilde{\Re} + \frac{1}{\mathrm{Re}}\left[\frac{1}{\tilde{r}}\frac{\partial}{\partial\tilde{r}}\left(\tilde{r}\frac{\partial\tilde{w}}{\partial\tilde{r}}\right) + \frac{1}{\tilde{r}^2}\frac{\partial^2\tilde{w}}{\partial\theta^2}\right]. \tag{17}$$

The rotor is at $\tilde{r} = \tilde{a}$ and the outer boundary $\tilde{r} = \tilde{b}$ and $\tilde{c} = 1$. The equation defining the stator surface is

$$\tilde{\Delta}(\theta) = \left(\tilde{b}^2 - (\tilde{e}\sin\theta)^2\right)^{1/2} - \tilde{e}\cos\theta \tag{18}$$

and

$$\tilde{e} = 1 - \tilde{\delta}\,. \tag{19}$$

The boundary conditions (8) hold for $\tilde{v},\tilde{u},\tilde{w},\tilde{p}$ and

$$\tilde{U}(\tilde{a},\theta) = 1 \tag{20}$$

The pressure gradient $\tilde{\Re}$ may be chosen to satisfy a prescribed pressure drop in the finite instrument. Equations (15) through (20) show that the problem for the planar motion is then completely characterized by two dimensionless parameters, the Reynolds number

$$\mathrm{Re} = Uc / \nu \tag{21}$$

and the eccentricity ratio

$$\tilde{e} = 1 - \tilde{\delta} \tag{22}$$

For the axial motion, the parameter $\tilde{\Re}$ must also be prescribed.

4 Numerical method

The equations (1) through (5) were solved by the numerical package SIMPLER in a routine application of techniques described by Patankar [1], which will not be repeated in detail here. The grid array used in the calculation is shown in figure 2. The motion of the fluid in the shaded region is suppressed by prescribing a very large viscosity there; motion is blocked by this artifice. Polar coordinates are appropriate for the annular region between the rotor and outer boundary; the stator is defined by the border of the blocked region according to equation (11).

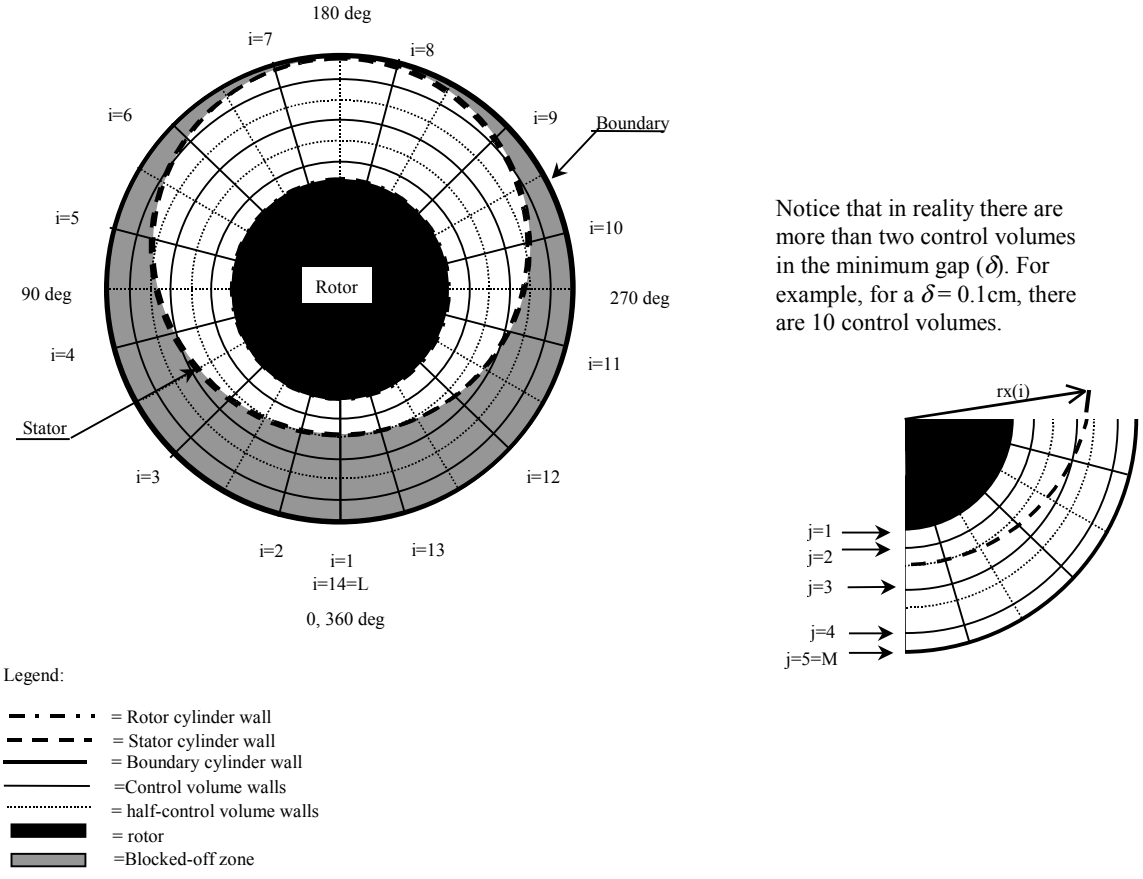

*Figure 2. Grid array. In this figure (*L,M*) = (14,5). In the computation (*L,M*) = (128,60).*

The grid is divided into L angular segments indexed by i and the nodes are defined by points on rays, indexed by j, $1 \leq j \leq M$. The distance between the radial nodes is uniform except for the nodes nearest to the stator and rotor. The calculations were carried out using numerical values typical of the EQM; in all the calculations $\rho = 1$ g/cc, $\mu = 0.2$ Pa•s, $a = 1.27$ cm, $b = 1.635$ cm.

The results of the calculations are not restricted to the numerical values used in the computations; particular numerical results may be re-expressed in terms dimensionless parameters giving families of values which express scaling of geometry speed and material parameters of maximum generality.

Table 1 lists values of the eccentricity and gap used in the calculation.

e (cm)	δ (cm)	$\tilde{e} = 1 - \tilde{\delta}$
0.265	0.100	0.726
0.165	0.200	0.452
0.065	0.300	0.178
0.0	0.365	0.0

Table 1. Eccentricities and eccentricity ratios studied in the simulation.

In table 2 we list the values of the velocity of the rotor used in the simulation.

Ω (rpm)	U = (cm/s)	Reynolds number Re = $\rho c U/\mu$
75.2	10.0	1.8
752.0	100.0	18.2
7,518.1	800.0	146
12,030.6	1600.0	292

Table 2. Speeds and Reynolds number used in the simulation.

5 Streamlines

Figure 3 shows that an eddy develops at a constant Reynolds number as the eccentricity increases past a critical value (*c*). At this relatively high Re, the eddy is not symmetric and shifts in the direction of rotation (*c.f.* figure 4). The flow at large $\tilde{e}$ is partitioned into eddy flow, which does not pass through the minimum gap and through flow, near the rotor.

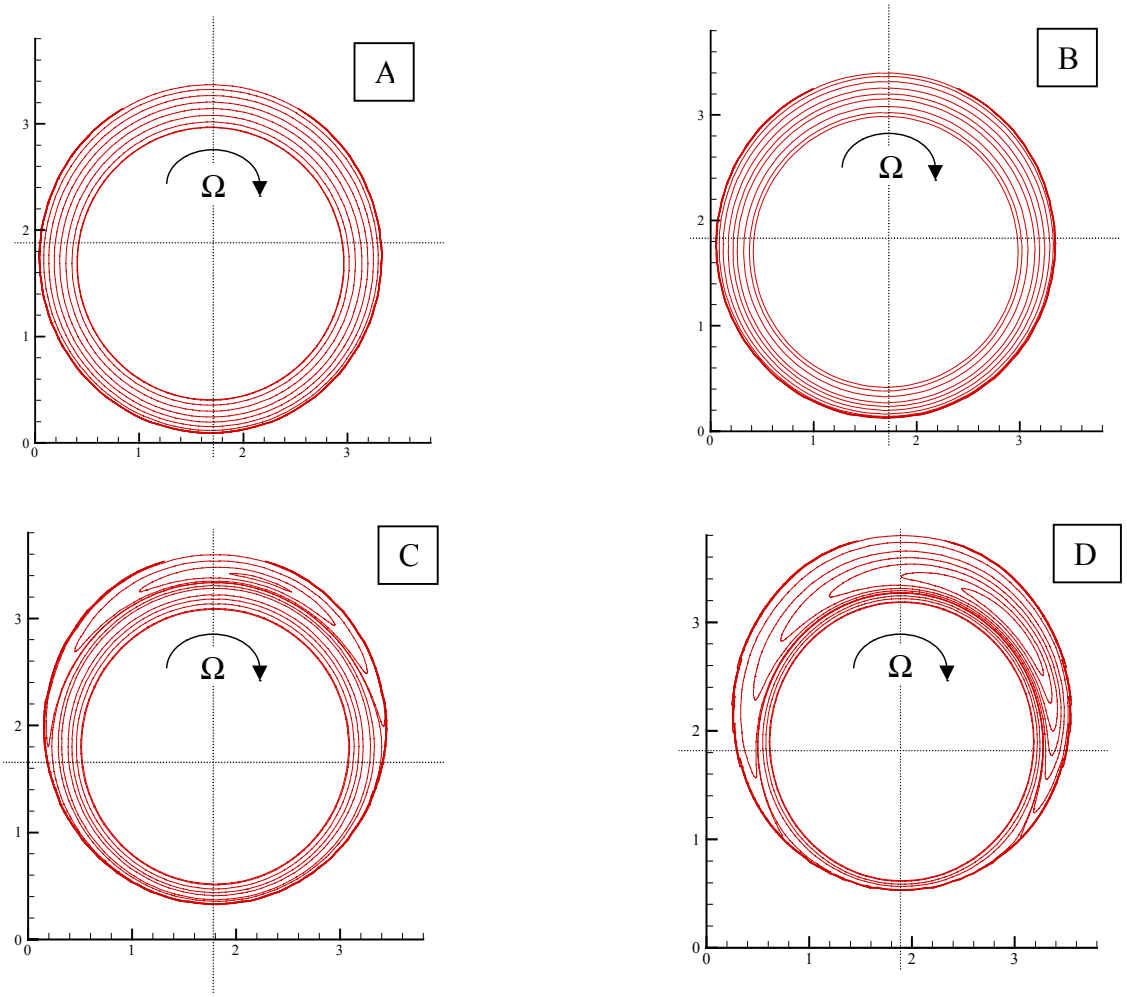

Figure 3. Streamlines for Re = 160 (A) $\tilde{e}$ = 0 (B) $\tilde{e}$ = 0.178 (C) $\tilde{e}$ = 0.452 (D) $\tilde{e}$ = 0.726.

Figure 4 shows that the eddy position does not shift much with eccentricity when the Reynolds number is close to zero. For Stokes flow the eddy is symmetric at all values of Re (Wannier [4]).

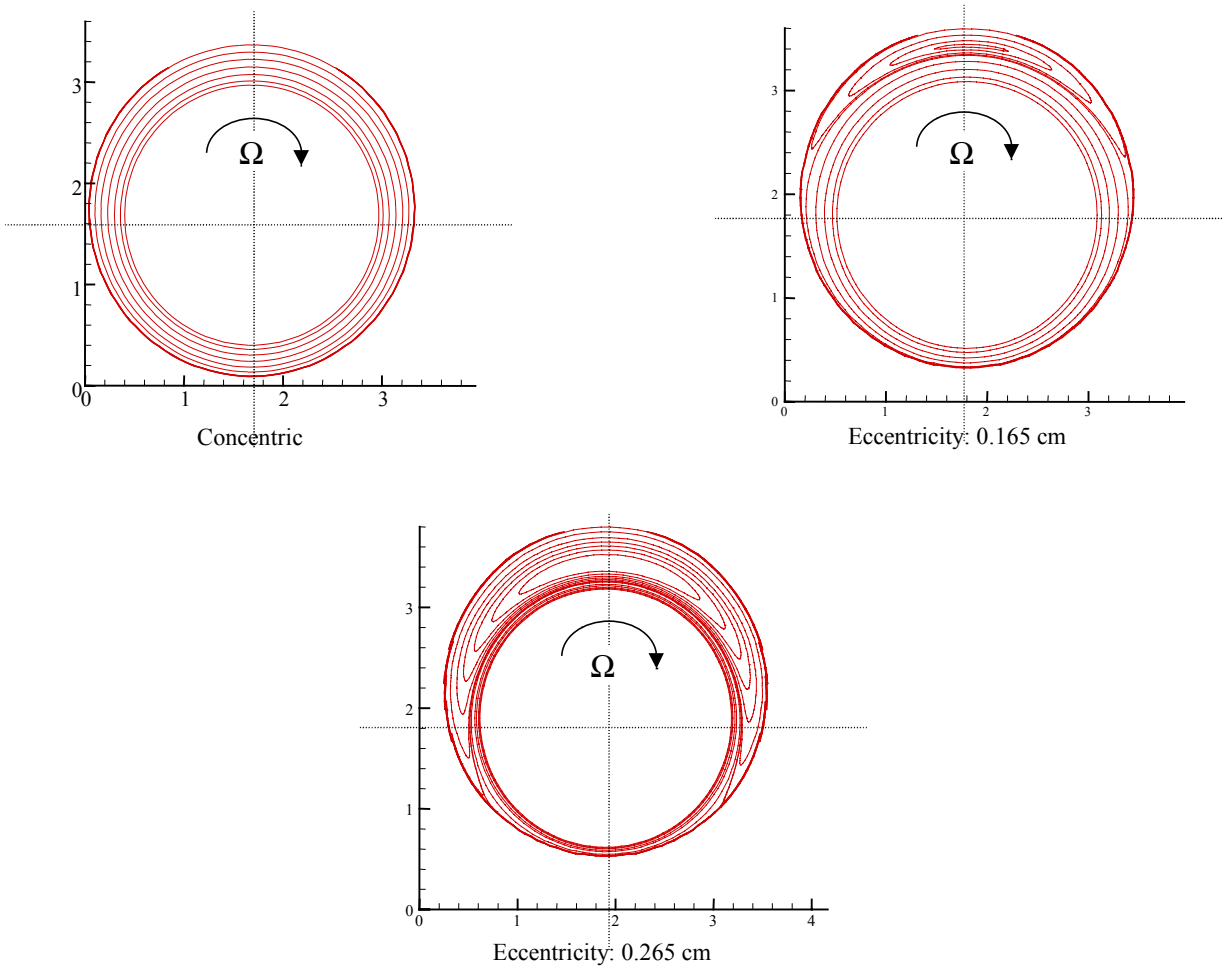

Figure 4. Streamlines at low Reynolds numbers Re = 1.8 and different eccentricities (table 1).

Figure 5 shows that the eddy grows and is shifted in the direction of rotation as the Reynolds number increased when $\tilde{e} = 0.452$ is fixed.

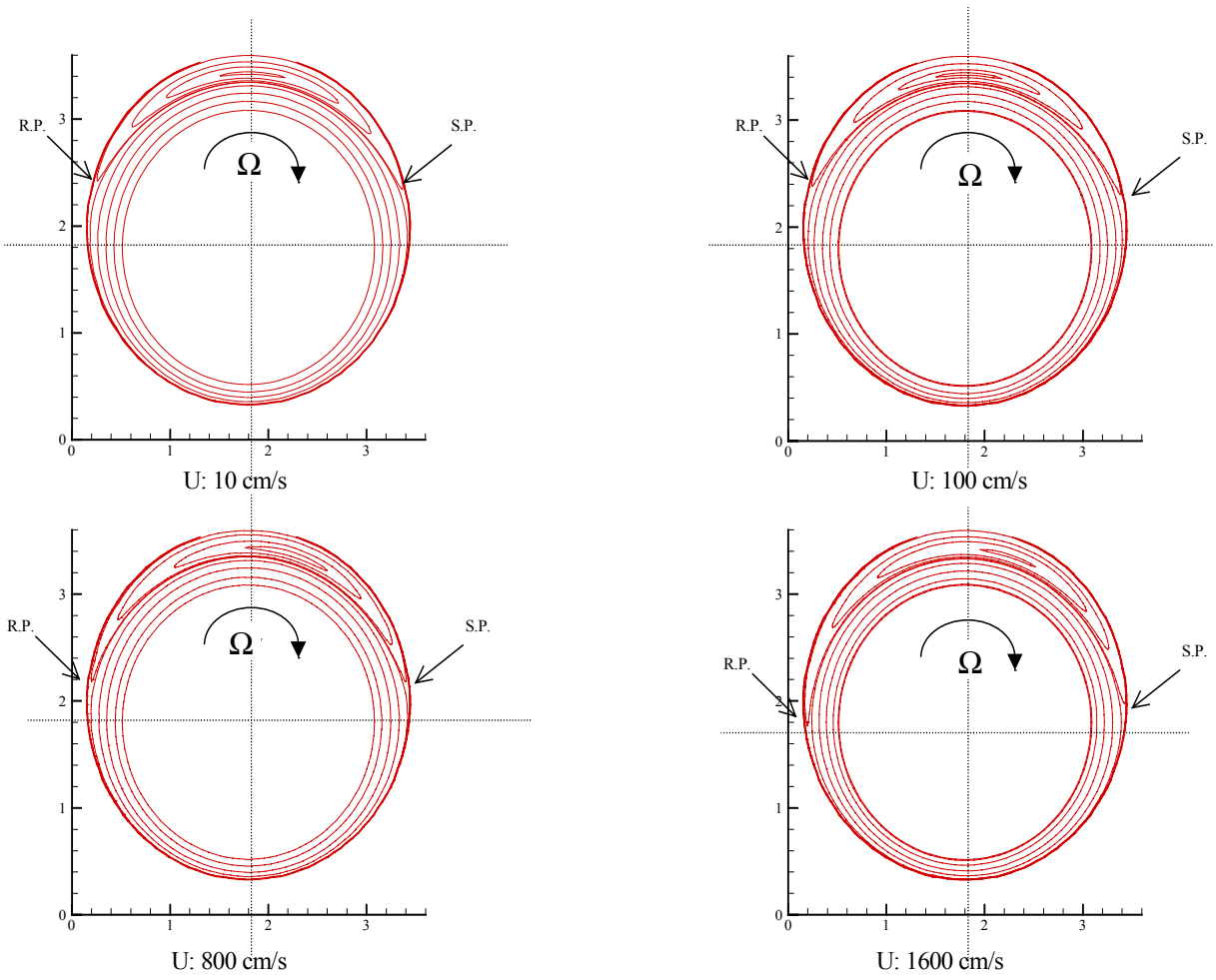

Figure 5. Streamlines for $\tilde{e}$ =0.452: (A) Re = 1.8, (B) Re = 18.2, (C) Re = 146, (D) Re = 292. The points of separation are designated as S.P.; points of re-attachment are designated as R.P.

Szeri [5] notes that streamlines are nearly circular for small eccentricities, but the pressure gradients which develop as eccentricity is increased cause the fluid to reverse direction near the stationary cylinder. Fluid in the recirculation zones do not pass through the small gap. Almost all the fluid is trapped in the eddy when the gap between the rotor and cylinder tends to zero.

The flow pattern just described has an application to the operation of EQM described in figure 1. In this instrument we test the stability of concentrated emulsions of heavy oil in water. The highly viscous dispersed oil phase can be modeled using solid particles. Particles injected at the upper side of the system (inlet port placed at the eddy region) will circle in the eddy and will not cross the minimum gap. But if particles are injected directly in the minimum gap, they will be milled and exposed to the largest pressure drop in the system. Therefore, the best location for the inlet port is at the bottom of the cylinder (0 degrees); with this configuration the particles can

follow the streamlines located close to the rotor and cycle repeatedly through the gap, where they will be milled.

On the other hand, for the outlet port location, the best place is at any region of positive pressure, but as far as possible from the eddy, so we get a quality sample that contains the particles that have been milled previously. It is important to notice that for large eccentricities the location of the outlet port seems not so easily set, since the eddy can take most of the space between rotor and stator.

In figure 6 we have plotted the axial velocity profile for the three eccentric positions in table 1 when the rotor surface speed of 1600 cm/s and an axial pressure gradient corresponding to a pressure drop of approximately 41.4 kPa at the ports in figure 1; the pressure gradient is $\Re$ = 89349 dyn/cm^3.

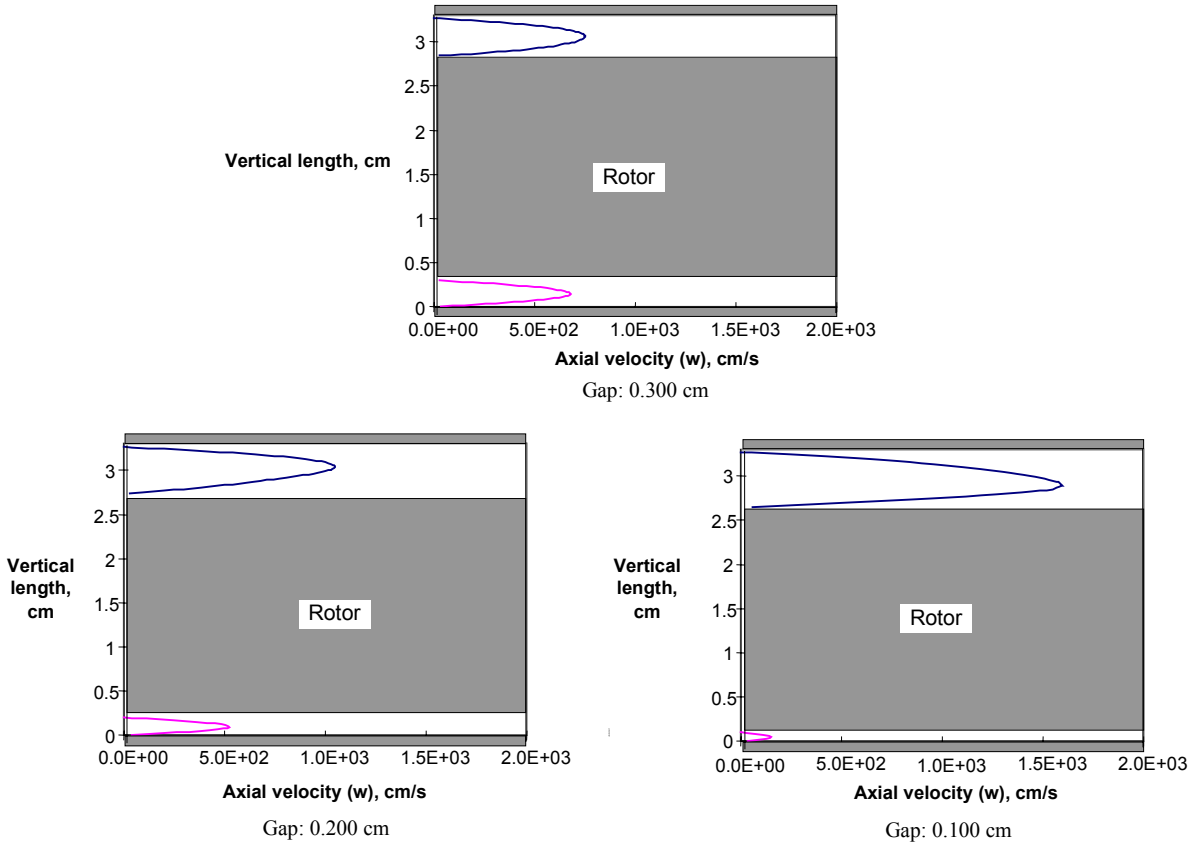

Figure 6. Effect of eccentricity on the axial velocity profile at ΩR = 1600 cm/s and ΔP: 41.4 kPa.

6 Relative pressure

Figure 7 shows pressure distributions for three different eccentricities; 0.065, 0.165 and 0.265 cm and for the rotor velocities shown in Table 2. For the lowest velocity and Reynolds number (A) the pressure distribution is almost symmetric with respect to the line of centers ($\theta = 0$), since the effect of fluid inertia is very low. On the other hand, when the speed of the rotor is increased, the effect of fluid inertia is to decrease the values of the negative pressure relative to that at $\theta = 0$, as shown in (B), (C) and (D).

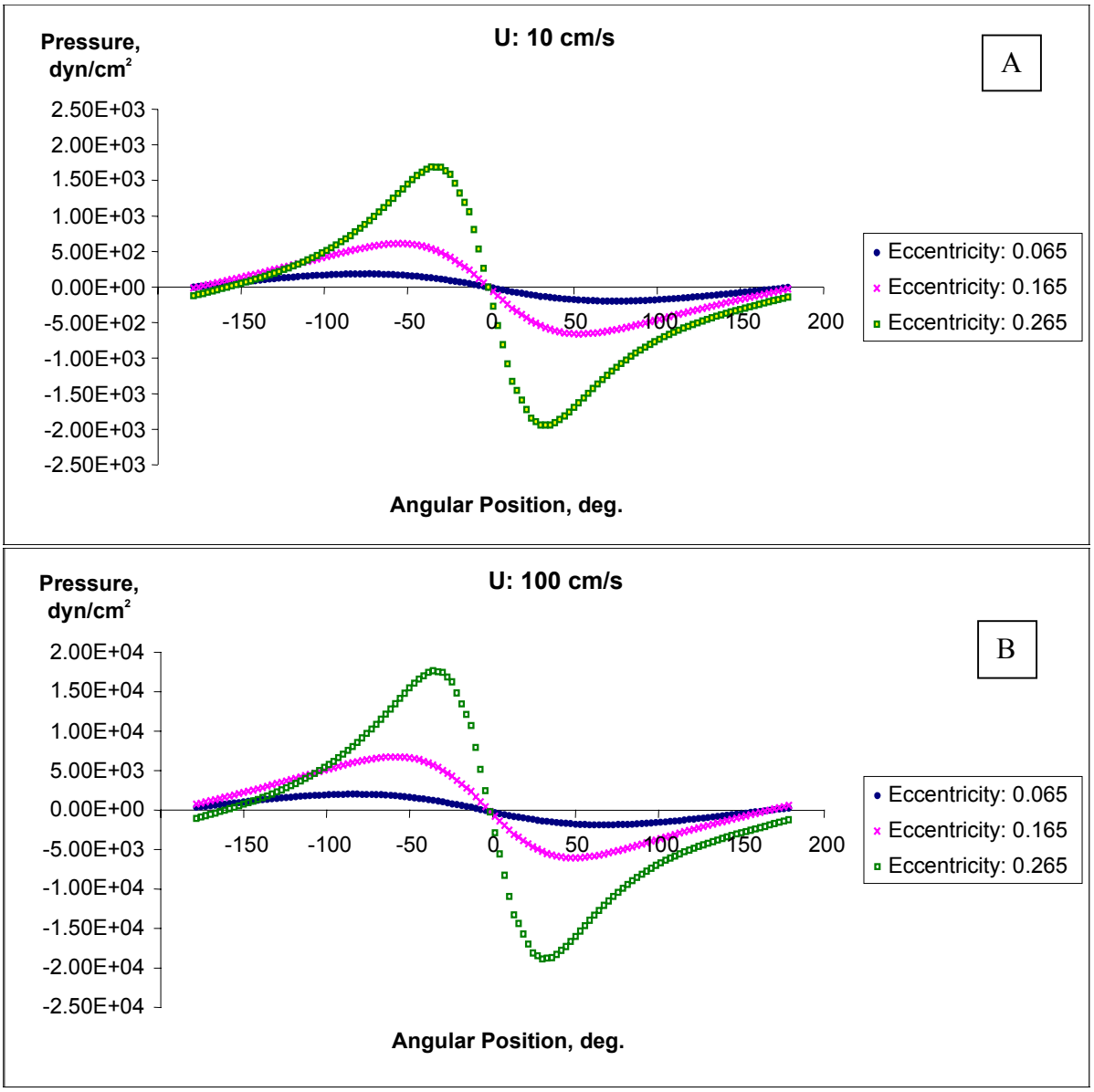

Figure 7-A,B. Average pressure distribution in function of angular position. A: 10 cm/s and B: 100 cm/s. The average is taken over radial nodes.

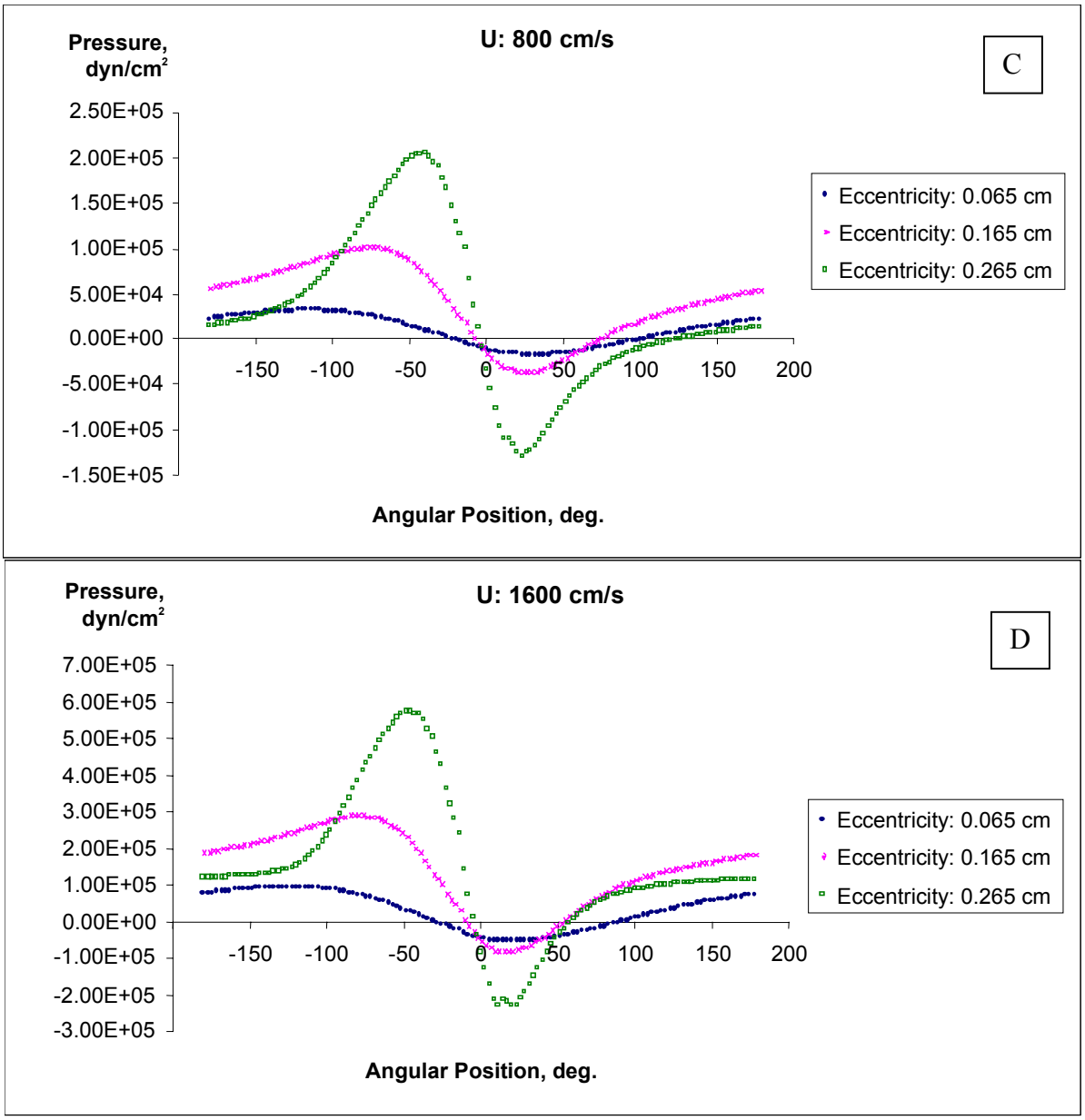

Figure 7-C,D. Average pressure distribution in function of angular position. C: 800 cm/s and D: 1600 cm/s. (See table 1 and 2 for dimensionless values.)

Figure 8 plots the absolute values of the maximum and minimum average pressure for e = 0.265 cm, the average is taken on rays from the origin and the maximum and minimum of these radial averages are found as a function of θ. The extreme values increase strongly with velocity (Reynolds number, see table 2.)

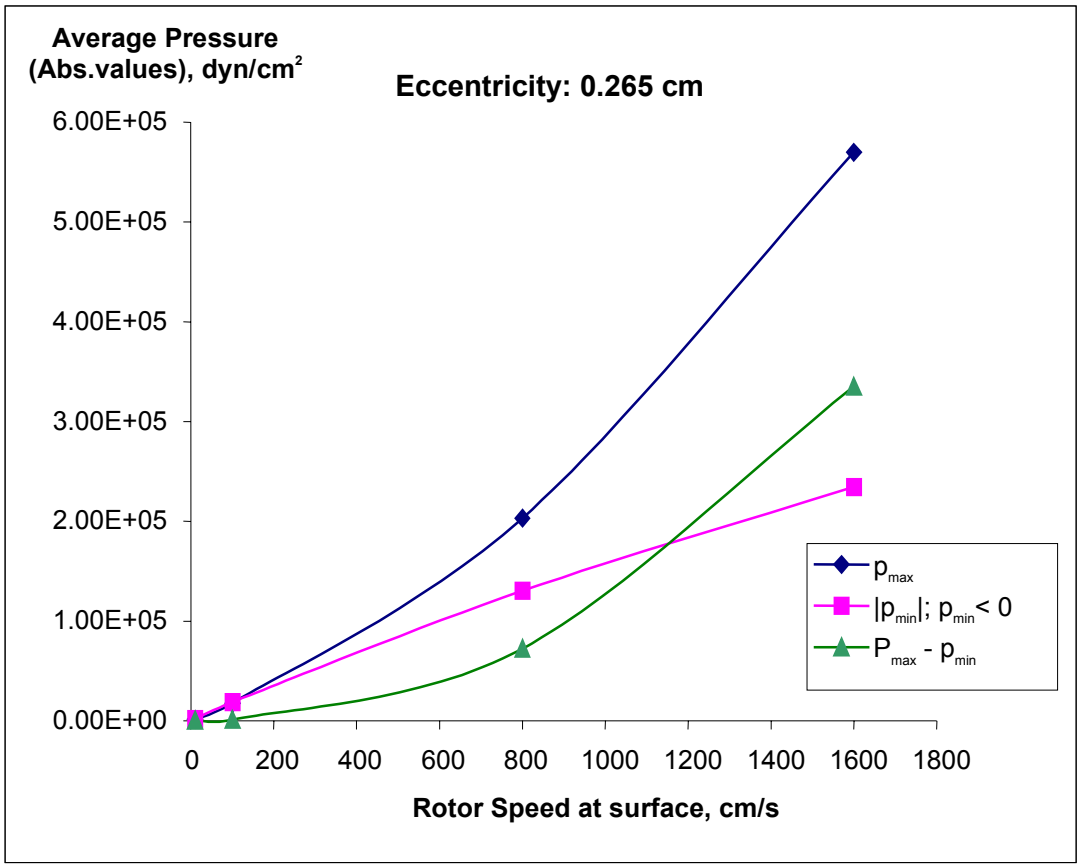

Figure 8. Largest/lowest average pressure and its difference vs. rotor speed (eccentricity: 0.265 cm). (See tables 1 and 2 for dimensionless values.)

Figure 8 demonstrates two important facts: first, when the speed is increased, the magnitude of both the negative (P_{min}) and positive pressure (P_{max}) increases; in other words, the pressure drop produced by the restriction becomes significantly higher. For smaller eccentricities, say 0.065 cm, the pressures still increases with speed, but the effect is less strong.

The second fact is that the differences between maximum and minimum pressure become large as the speed increases. As we pointed out before, this is due to inertia. For low speeds, the difference between the maximum and minimum pressure is small because the inertia of the fluid does not play in important role.

The effect of speed on negative pressure is shown by figures 7A-D. At 10 cm/s the angles covered by negative pressure is about 202 degrees; this range decreases considerably as the speed is increased, e.g. 157 degrees at 100 cm/s, then 128 degrees at 800 cm/s and finally only 58 degrees at 1600 cm/s.

Another important feature is the behavior of pressure gradient $dp/d\theta$ between the highest and lowest pressure; this is given by $\Delta p/arc\ length$ where $\Delta p = p_{max} - p_{min}$. This pressure gradient is plotted as a function of speed at an eccentricity of 0.265 cm in figure 9.

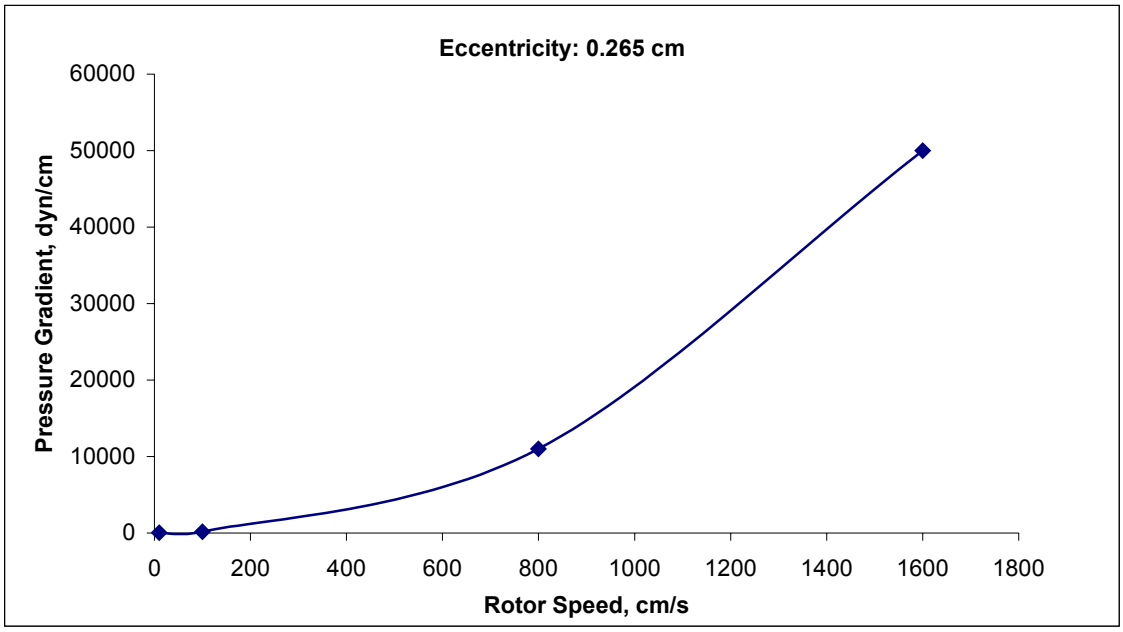

Figure 9. Pressure gradient at different speeds, using an eccentricity of 0.265 cm.

7 Comparison of pressure, shear and viscous normal stresses

The rate of strain tensor in polar coordinates is given by

$$
\begin{aligned}
D_{rr} &= \frac{\partial v}{\partial r} & D_{r\theta} &= \frac{1}{2}\left[r\frac{\partial}{\partial r}\left(\frac{u}{r}\right) + \frac{1}{r}\frac{\partial v}{\partial \theta}\right] & D_{rz} &= \frac{1}{2}\left[\frac{\partial v}{\partial z} + \frac{\partial w}{\partial r}\right] \\
D_{\theta r} &= \frac{1}{2}\left[r\frac{\partial}{\partial r}\left(\frac{u}{r}\right) + \frac{1}{r}\frac{\partial v}{\partial \theta}\right] & D_{\theta\theta} &= \frac{1}{r}\frac{\partial u}{\partial \theta} + \frac{v}{r} & D_{\theta z} &= \frac{1}{2}\left[\frac{1}{r}\frac{\partial w}{\partial \theta} + \frac{\partial u}{\partial z}\right] \\
D_{zr} &= \frac{1}{2}\left[\frac{\partial v}{\partial z} + \frac{\partial w}{\partial r}\right] & D_{z\theta} &= \frac{1}{2}\left[\frac{1}{r}\frac{\partial w}{\partial \theta} + \frac{\partial u}{\partial z}\right] & D_{zz} &= \frac{\partial w}{\partial z}
\end{aligned}
\qquad (25)
$$

The components of the stress tensor in polar coordinates are 2μ times the components of the rate of strain tensor.

Figure 10 A, B shows the shear stress ($\tau_{r\theta}$) and the extensional stress ($\tau_{\theta\theta}$) vs. angle in an interval around the minimum gap. Here the rotor speed is 1600 cm/s for three different eccentricities, 0.065, 0.165 and 0.265 cm. Figure 11 shows that the shear stress grows as the eccentricity is increased.

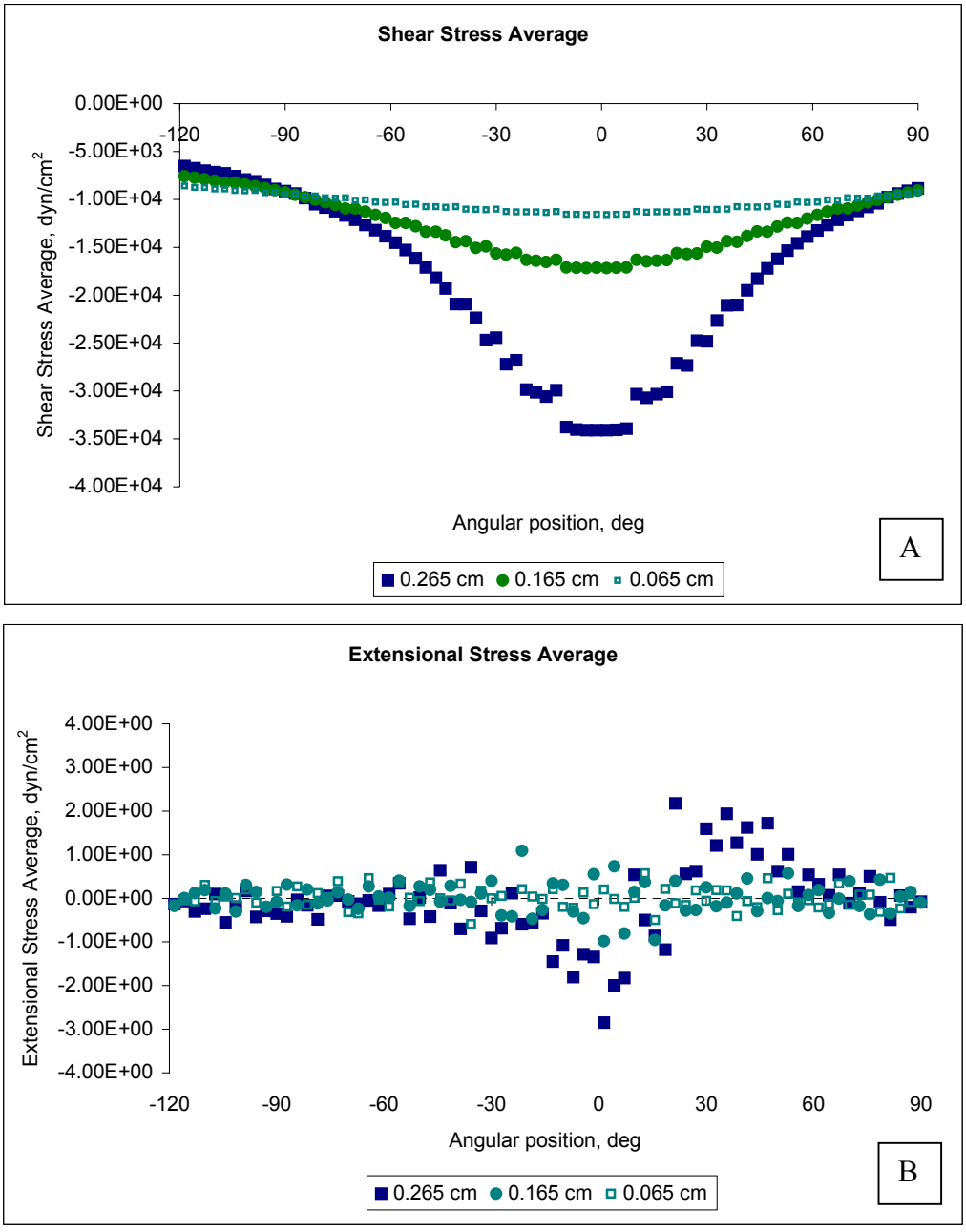

Figure 10. Effect of eccentricity on stress A: shear stress ($\tau_{r\theta}$), *B: extensional stress* ($\tau_{\theta\theta}$), $\Omega R = 1600$ *cm/s.*

Figure 11 shows the tangential velocity distribution for three different eccentricities with the same velocity of rotation; $\partial u/\partial r$ increases with the eccentricity. This is the reason that the shear stress increases with eccentricity.

Comparison of figures 10A and 10B shows that the extensional stress is much smaller than the shear stress; about four orders of magnitude smaller. The extensional stress is based principally on the variation of the tangential velocity with respect to the angular distance which is only slowly varying (see figure 12.)

The scatter in figure 10B is possibly due to numerical error since relatively small values are calculated by numerical differentiation. This may indicate that the grid refinement was not sufficient for this quantity, however this does not detract from the conclusion as to the dominant stress in the flow since the differences are greater than an order of magnitude.

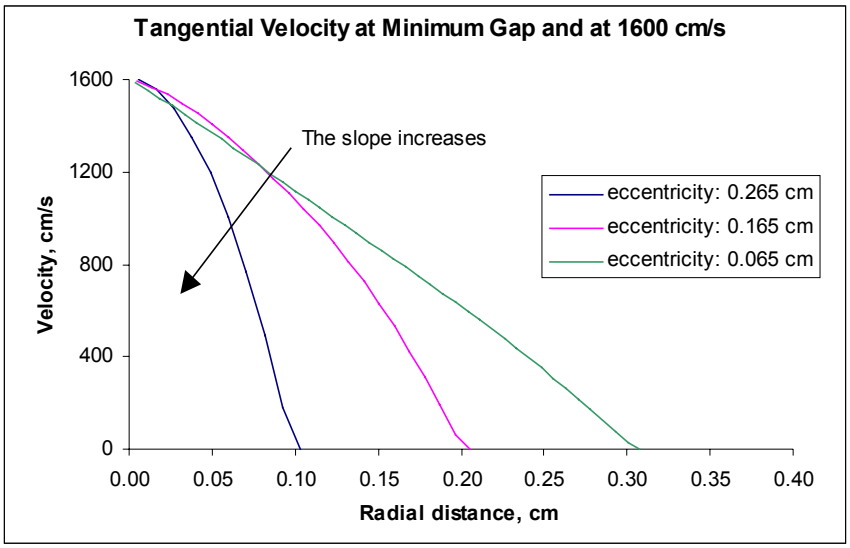

Figure 11. Tangential velocity distribution vs. radial distance in the minimum gap for three different eccentricities, ΩR *= 1600 cm/s.*

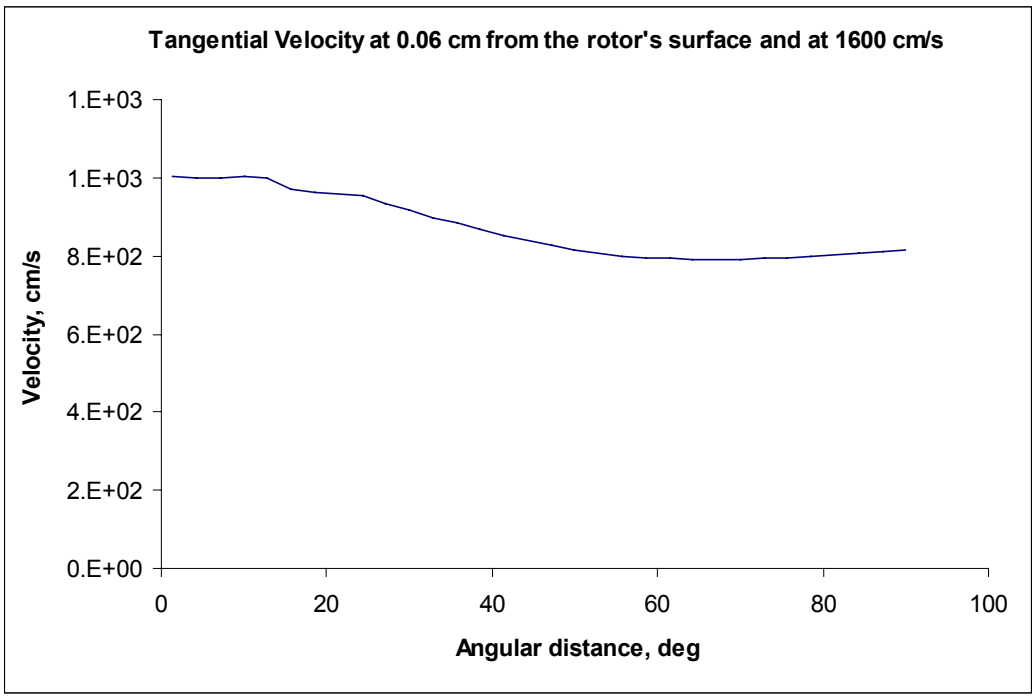

Figure 12. Tangential velocity distribution vs. angular distance (0-90 deg.), at a radial distance of 0.06 cm measured from the rotor's surface.

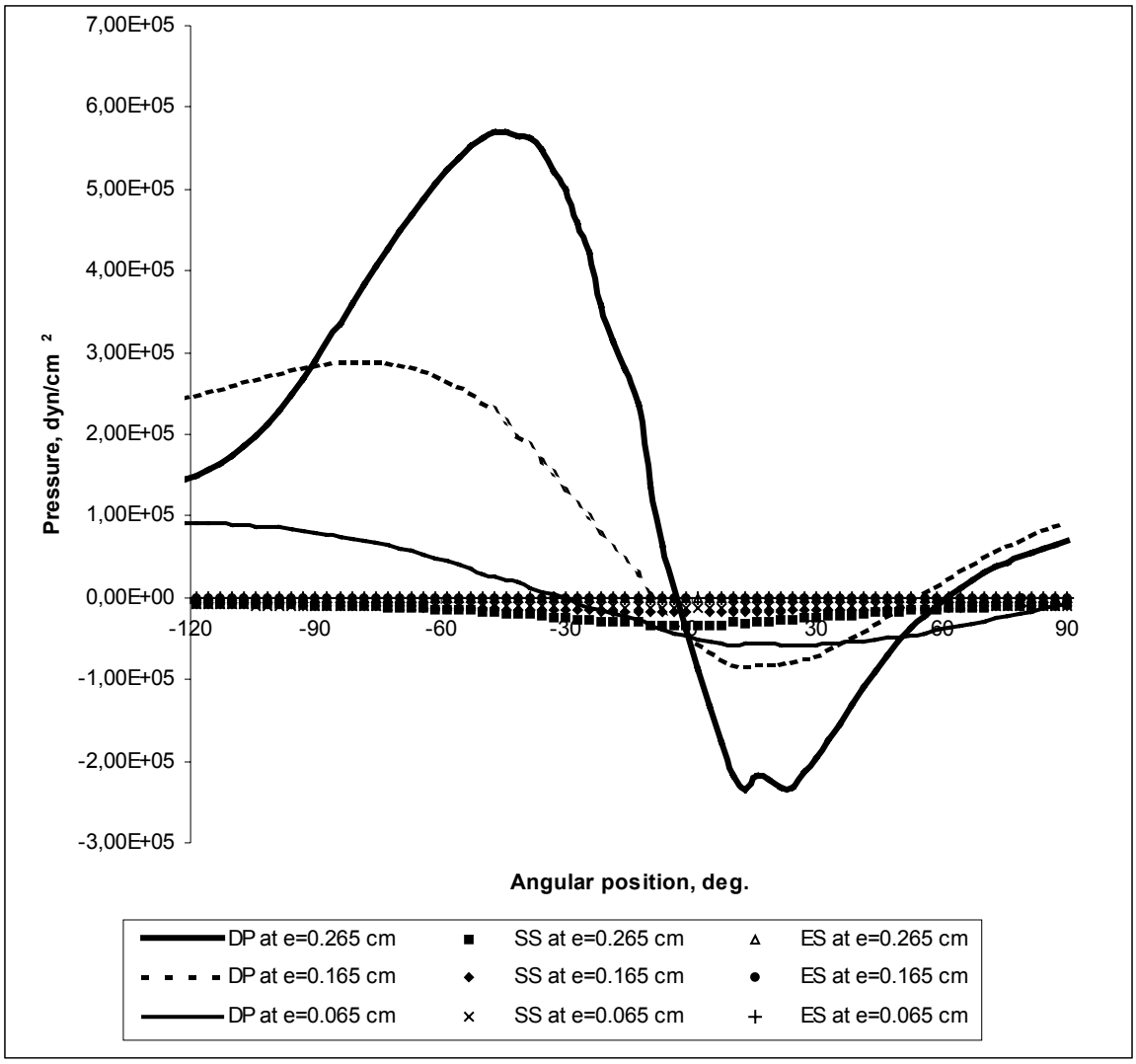

Figure 13 Dynamic pressure average (DP), shear stress average (SS) and extensional stress (ES) average vs. angle for three eccentricities, $\Omega R = 1600$ cm/s.

Now we will make some comparisons between the shear stress, the extensional stress and the dynamic pressure for a tangential velocity of 1600 cm/s and three different eccentricities (figure 13). The magnitude of the dynamic pressure (DP) is considerably higher than the shear (SS) and extensional stress (ES) for configurations associated with the same eccentricity and all angles. We may conclude that the pressure gradient between the extreme values of the pressure is the major force at play in flow between eccentric rotating cylinders.

Although the values of shear stress do not change much for small angles near zero, the dynamic pressure is smaller than the shear stress at some points, therefore the flow deformation could be governed by the local shear stress in these locations. However, the shear stress and dynamic pressure are *both* of $O(10^4)$ dyn/cm^2, for this configuration.

8 Torque and mechanical power

Since we have already calculated the shear stresses across the gap and for every angular position, we can use the shear stress at the wall of the rotor to estimate the theoretical torque

$$T = 2\pi a^2 L \bar{\tau}_{r\theta}$$

where $\bar{\tau}_{r\theta}$ is the average over $0 \le \theta \le 2\pi$ of $\tau_{r\theta}(a,\theta)$. Figure 14A gives T vs $U = \Omega a$ for different eccentricities.

The mechanical power required to turn the rotor is given

$$P = TW.$$

P is the mechanical power in watts, T is the torque calculated previously in N*m and W is the angular velocity in rad/s. Figure 14B gives P vs. Ω for every eccentricity speed range specified in this work.

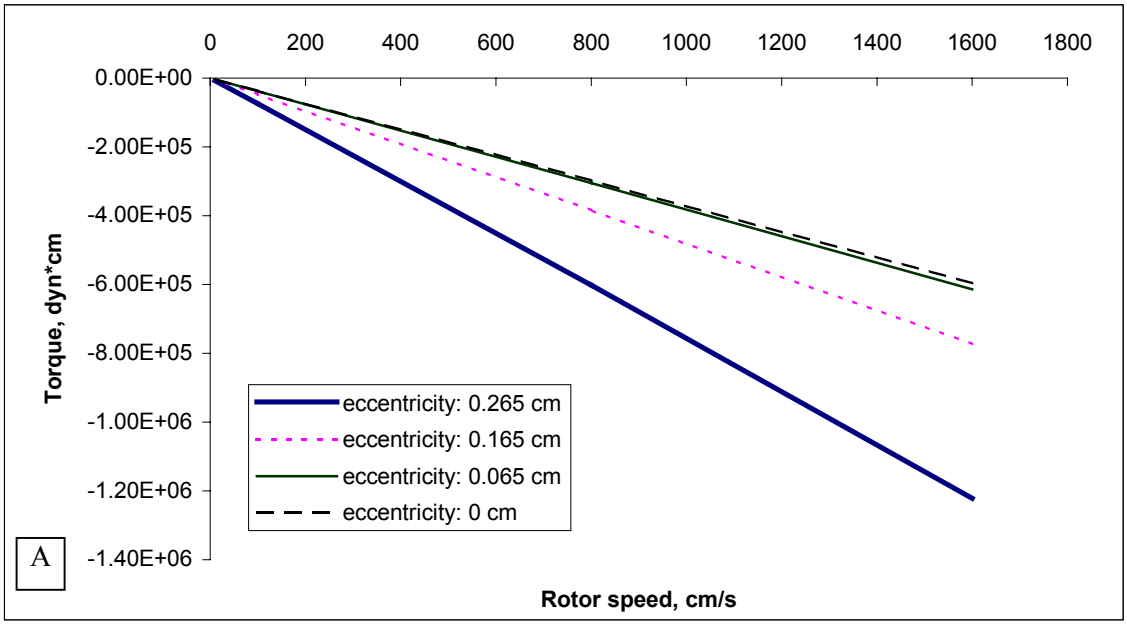

Figure 14A. Torque vs. rotor speed for $\Omega a = 10$, 100, 800 and 1600 cm/s and eccentricities: 0.265, 0.165, 0.065 and 0 cm (concentric).

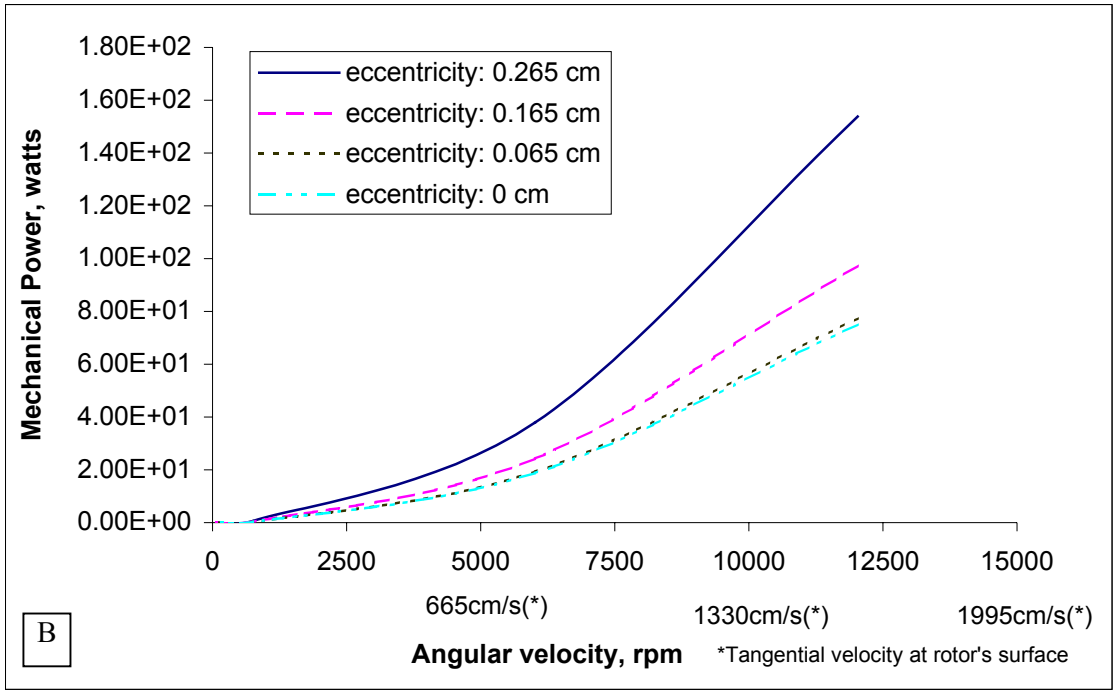

Figure 14B. Mechanical power as a function of angular velocity and eccentricity.

9 Lubrication approximation

As we have seen previously, the solutions of the full Navier-Stokes equations and continuity equations are far from elementary, and in some applications there are ways to simplify these equations. Such simplification is made particularly easy in lubrication theory due to the geometry of lubricant films: under normal conditions the in-plane dimension of the film is significantly greater than its thickness. It is further assumed that the Reynolds number is very small so that inertia may be neglected. Under these assumptions, Osborne Reynolds derived his celebrated lubrication equation for the relative pressure $p(r,\theta)$

$$\frac{d}{d\theta}\left(h^3\frac{dp}{d\theta}\right)+6\mu Ua\frac{dh}{d\theta}=0 \tag{26}$$

where

$$h(\theta)=\delta-e\cos\theta \tag{27}$$

The solution of (26) and (27) which is periodic in θ with period 2π was given by Reynolds as

$$p-p_r=\frac{6\mu UR}{\delta^2}\cdot\frac{\varepsilon}{2+\varepsilon^2}\cdot\frac{\sin\theta(2-\varepsilon\cos\theta)}{(1-\varepsilon\cos\theta)^2}\ , \tag{28}$$

where $\varepsilon = e/\delta$. The positions of the maximum and minimum pressures are found in the standard way and are presented in tables 3 and 4.

ε	h_m/δ	$\theta_m(\text{deg})$	$h_{\min}/h_{\max}$
0.00	1.000	90.0	1.000
0.10	0.985	81.4	0.818
0.18	0.953	74.8	0.698
0.20	0.941	72.9	0.667
0.30	0.871	64.5	0.538
0.40	0.778	56.3	0.429
0.45	0.722	52.0	0.377
0.50	0.667	48.2	0.333
0.60	0.542	40.3	0.250
0.70	0.410	32.5	0.176
0.73	0.374	30.5	0.159
0.80	0.273	24.6	0.111
0.90	0.135	16.1	0.053
1.00	0.000	0.0	0.000

Table 3. Film thickness (h_m), angular position (θ_m) at max/min pressure, and ratio between min. and max. film thickness ($h_{\min}/h_{\max}$) for different ε.

ε	$e(cm)$	$h_m(cm)$	$\theta_m(\text{deg})$	$h_{\max}(cm)$	$h_{\min}(cm)$
0.00	**0.000**	**0.365**	**90.0**	**0.365**	**0.365**
0.10	0.037	0.360	81.4	0.402	0.329
0.18	**0.065**	**0.348**	**74.8**	**0.430**	**0.300**
0.20	0.073	0.344	72.9	0.438	0.292
0.30	0.110	0.318	64.5	0.475	0.256
0.40	0.146	0.284	56.3	0.511	0.219
0.45	**0.165**	**0.263**	**52.0**	**0.530**	**0.200**
0.50	0.183	0.243	48.2	0.548	0.183
0.60	0.219	0.198	40.3	0.584	0.146
0.70	0.256	0.150	32.5	0.621	0.110
0.73	**0.265**	**0.137**	**30.5**	**0.630**	**0.100**
0.80	0.292	0.100	24.6	0.657	0.073
0.90	0.329	0.049	16.1	0.694	0.037
1.00	0.365	0.000	0.0	0.730	0.000

Bold letters are for the four cases in our study

Table 4. Film thickness (h_m) and angular position (θ_m) at points of maximum or minimum pressure for different ε, when $\delta = 0.365cm$. $h_{\min}$ and $h_{\max}$ are gap sizes on the center line ($\theta = 0$).

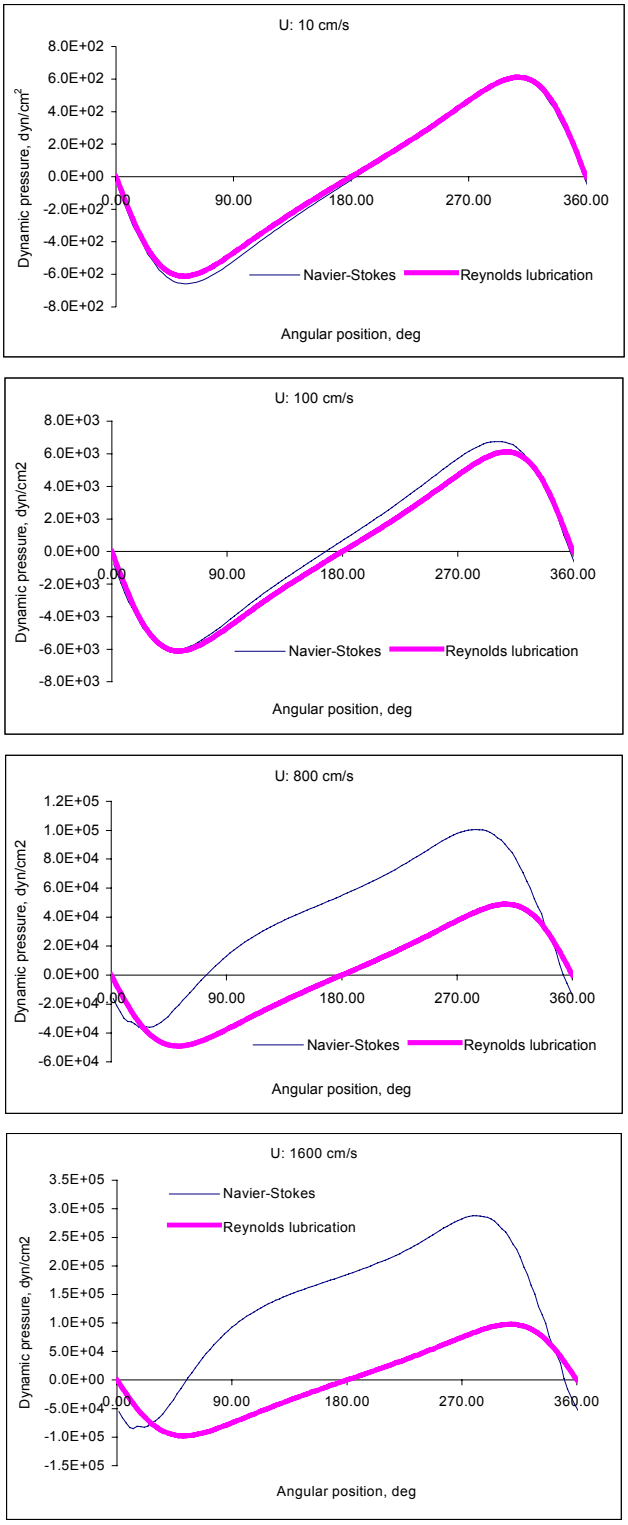

Figure 15. Comparison of the pressure distribution by simulation with the lubrication pressure (28) for different speeds when e *= 0.165 cm.*

In figure 15 we compare the pressure distribution given by (28) with an average pressure $\overline{p}(\theta)$ obtained from simulated pressure $p(r,\theta)$ by averaging over r for different speeds (Reynolds number, see table 2) when the eccentricity is 0.165 cm (see table 1). The effects of inertia are dramatic; the zero of $\overline{p}(\theta)$ migrates in the direction opposite to rotation while the eddies are shifted in the direction of rotation. The magnitude of the pressure and the symmetry of distribution is very sensitive to the Reynolds number.

10 Stress induced cavitation

Joseph [3] proposed a cavitation criterion which is based on the idea that the state of stress at each point in a moving fluid is determined by the principal tensile stress and not by the pressure. Even though the criterion for cavitation ought to be based on the principal stresses and not the pressure, it is useful to introduce a pressure as the mean normal stress as in a Newtonian fluid

$$\mathbf{T} = -\pi\mathbf{1} + \mathbf{S},\ \ \mathbf{S} = 2\mu\mathbf{D}[\mathbf{u}] \tag{29}$$

where $\pi = p_{abs}$ is the absolute pressure, $\mathbf{S}$ is the stress deviatoric stress tensor and D is the rate of strain tensor.

$$\pi = -\frac{1}{3}\text{Trace}\,\mathbf{T},\ \text{Trace}\,\mathbf{S} = S_{11} + S_{22} + S_{33} = 0\,. \tag{30}$$

Since $S_{11} \geq S_{33} \geq S_{22}$ we have

$$S_{11} > 0 \text{ and } S_{22} < 0 \tag{31}$$

where

$$S_{11} - S_{22} > 0 \tag{32}$$

is largest in the coordinate system in which $\mathbf{T}$ is diagonal.

Consider now the opening of a small cavity. It is hard to imagine very large differences in the pressure of vapor in the cavity so that the cavity should open in the direction where the tension is greatest. The idea that vapor cavities open to tension is endemic in the cavitation community, but it seems not to have been noticed before that this idea requires one to consider the state of stress at a point and, at the very least, to determine the special principal axes coordinates in which the tension is maximum. To remind us of this important point we shall call $\zeta(\psi)$ the special coordinate system in which the orthogonal transformation $\mathbf{Q}$ diagonalizes $\mathbf{T}$ (and $\mathbf{S}$):

$$\mathbf{Q}^T\mathbf{T}\mathbf{Q} = \text{diag}\,(T_{11}, T_{22}, T_{33}) \tag{33}$$

Here ψ in $\zeta(\psi)$ stands for the direction cosines in the diagonalizing transformation, and ψ is the diagonalizing angle for the two-dimensional rotation. The rotation of $\mathbf{T}$ is an important part of the theory of cavitation.

In two dimensions the components of the stress deviator in $\zeta(0)$ are given by

$$\left[\mathbf{S}\right]=\begin{bmatrix} S_{11} & S_{12} \\ S_{12} & -S_{11} \end{bmatrix}=2\mu\begin{bmatrix} D_{rr} & D_{r\theta} \\ D_{r\theta} & -D_{rr} \end{bmatrix} \tag{34}$$

The angle ψ that diagonalizes **S** is given by

$$\begin{cases} \sin 2\psi = S_{12}\Big/\sqrt{S_{12}^2+S_{11}^2}\,, \\ \cos 2\psi = S_{11}\Big/\sqrt{S_{12}^2+S_{11}^2} \end{cases} \tag{35}$$

and

$$[\mathbf{S}]=\sqrt{S_{12}^2+S_{11}^2}\begin{bmatrix} 1 & 0 \\ 0 & -1 \end{bmatrix}. \tag{36}$$

The largest stress component in the principal value coordinate system is

$$T_{11}+\frac{1}{2}\left(T_{11}+T_{22}\right)=S_{11}\,; \tag{37}$$

the smallest component is

$$T_{22}+\frac{1}{2}\left(T_{11}+T_{22}\right)=-S_{11} \tag{38}$$

and

$$T_{11}\text{ - }T_{22}=2S_{11} \tag{39}$$

We call T_{11} the maximum tension and T_{22} the minimum tension. If the maximum tension is negative, it is compressive; the minimum tension is even more compressive.

If a cavitation bubble opens up, it will open in the direction of maximum tension. Since this tension is found in the particular coordinate system in which the stress is diagonal, the opening direction is in the direction of maximum extension, even if the motion is a pure shear.

Examples of stress-induced cavitation and even of cavitation in pure shear were discussed by Joseph [3]. The numerical study of this paper can be used to apply the idea of stress induced cavitation to the problem of flow between eccentric rotating cylinders with throughput. Of particular interest is the comparison of

$$T_{11}=-\pi+S_{11} \tag{40}$$

with π alone; T_{11} has the effect of stress induced tension and $-\pi$ is an isotropic tension. In the theory of stress induced cavitation, a bubble will open when

$$T_{11}>-p_c \tag{41}$$

where p_c is a cavitation threshold, say the vapor pressure. Besides the difference in the magnitude of T_{11} and $-\pi$, the places where these quantities take their extreme values and the

angle of principal stresses are of interest; in our apparatus there is an axial flow which would be considered later. Even in the case of axial flow we neglected end effects.

First we shall consider the case when there is no axial flow; the problem is then two-dimensional and the principal stresses of the deviator are given by (36) using (34). In our numerical work we calculated the relative pressure $\pi = p + p_r(0)$. We may suppose that $p_r(0)$ and compare $-p$ to $T_{11} = -p + S_{11}$. The reference pressure may always be added back.

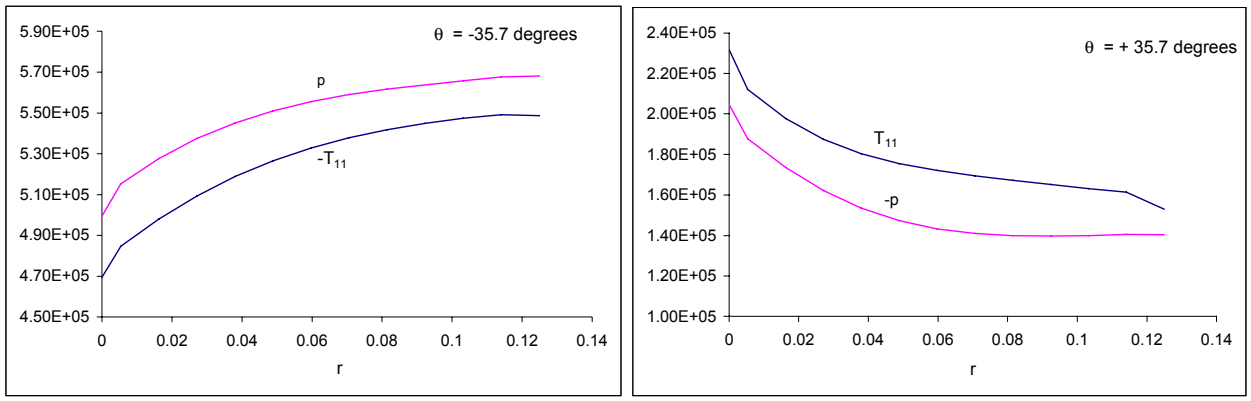

Figure 16. p *and* $-T_{11}$ *vs.* r *in the converging flow* θ = *-35.7 deg. and the diverging flow* θ = *35.7.*

In figure 16 we have plotted $-p$ and T_{11} as a function of r for two different angles 35.7 deg. (near the maximum of p), –35.7 deg. (near the minimum of p). The flow at the section $\theta = -35.7$ deg. is converging and $p > 0$, $T_{11} < 0$; we see that $-T_{11}$ is less compressive than p at all r and the smallest compression is at the rotor. The flow at the section $\theta = 35.7$ deg. is diverging and $p < 0$, $T_{11} > 0$; we see that T_{11} is more tensile than $-p$ at all r and the largest tension is at the rotor. The same features at all other angles not do close to $\theta = 0$. We may conclude that the most dangerous place for cavitation is at the rotor and that the cavitation is set by the motion, by the value of T_{11} which gives greater tension or less compression than p.

It follows now that we ought to look for cavitation sites on the rotor and on the rotor, at $r \to a$

$$D_{rr} = \frac{\partial v}{\partial r} = 0 \tag{42}$$

as a consequence of (1) and boundary condition. Since $D_{rr} = 0$, we are in a case of pure shear and the principal directions are at 45 deg. from the shearing direction.

The principal tensile stress T_{11} and pressure $-p$ are compared in figures 17, 18 and 19. The magnitude of the largest principal tensile stress is always smaller than the magnitude of the pressure since the tension due to motion is always additive. The inception of cavitation in a moving fluid is always stress induced.

The differences between T_{11} and $-p$ are larger at higher speeds (or Reynolds numbers, see tables 1 and 2). For example near the pressure minimum for speeds Ωa = 1600 cm/s in figure 19 we have differences of the order 10^4 dyn/cm^2, of the order of the vapor pressure 4.23×10^4 dyn/cm^2 at 30°C.

The position of the point of greatest tension is shifted slightly toward the origin by motion since the shear stress is greatest near $\theta = 0$.

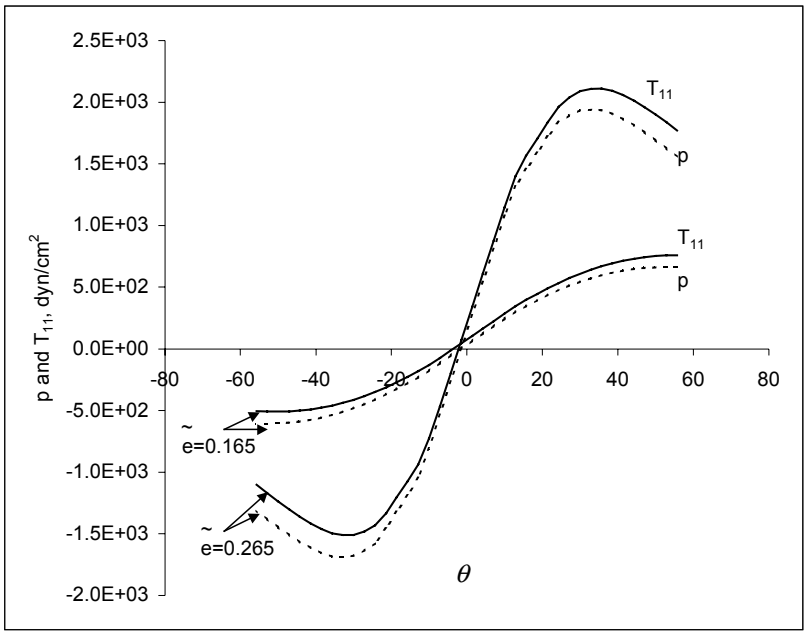

Figure 17. Comparison of tensile stresses –p *and* $T_{11} = -p + S_{11}$ *for* $\Omega a = 10$ *cm/s. Positive values are in the diverging zone with low pressures and high tensile stresses favorable to cavitation.*

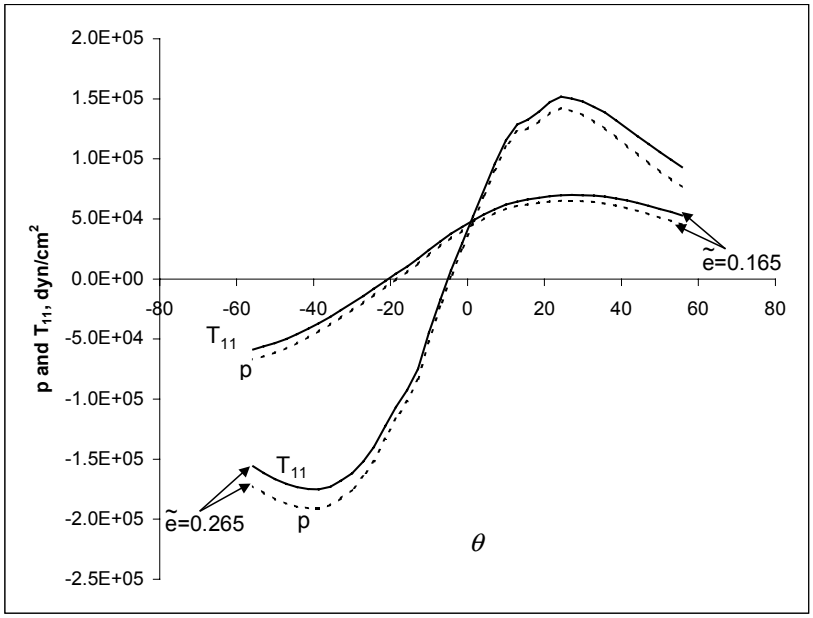

Figure 18. Comparison of tensile stresses –p *and* $T_{11} = -p + S_{11}$ *for* $\Omega a = 800$ *cm/s. Positive values are in the diverging zone with low pressures and high tensile stresses favorable to cavitation.*

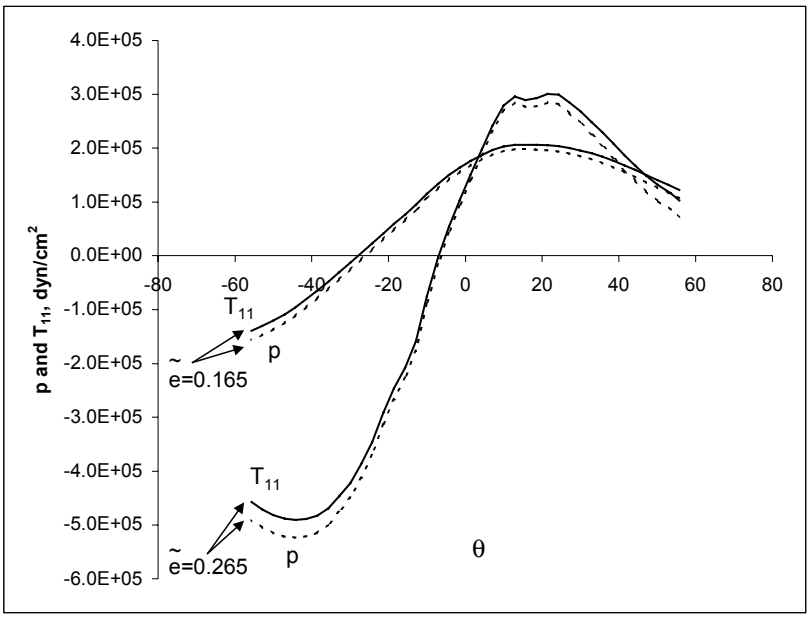

Figure 19. Comparison of tensile stresses $-p$ *and* $T_{11} = -p + S_{11}$ *for* $\Omega a = 1600$ *cm/s. Positive values are in the diverging zone with low pressures and high tensile stresses favorable to cavitation.*

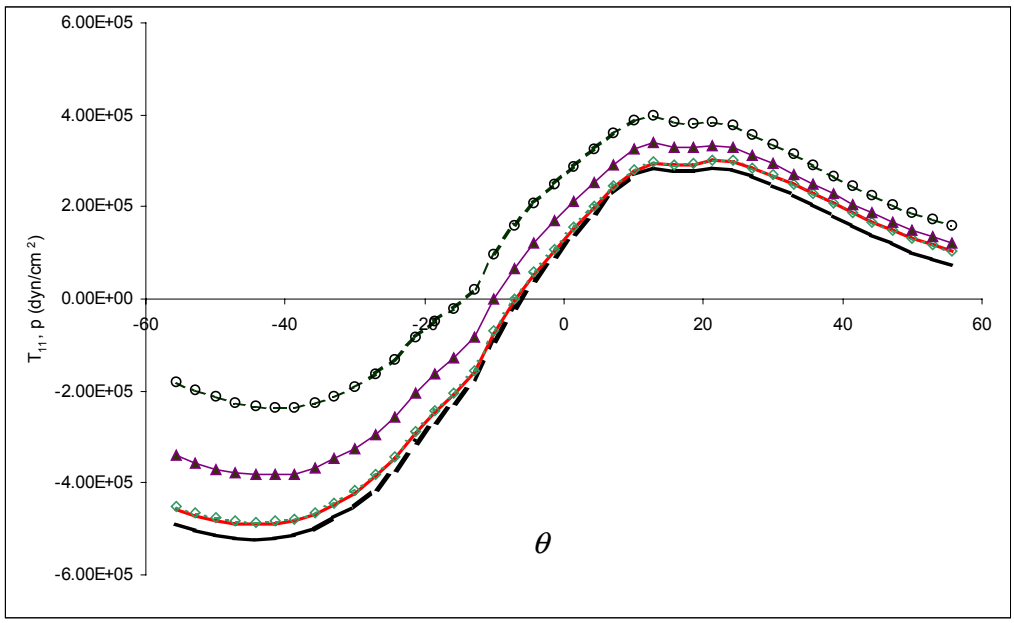

Figure 20. Comparison of $-p$ *and* T_{11} *for different axial pressure gradients* $\tilde{\Re}$ *corresponding to pressure drop* Δp*:* ▬ *pressure,* ▬ T_{11} *for* $\Delta p = 0$*,* ┈◇┈ T_{11} *for* $\Delta p = 41.4$ *kPa,* ▬▲▬ T_{11} *for* $\Delta p = 310.2$ *kPa, and* ▬⊙▬ T_{11} *for* $\Delta p = 655$ *kPa.*

We now consider the effects of axial motion on stress induced cavitation between rotating eccentric cylinders. The only non-zero stress for the axial motion is

$$2\mu D_{rz} = \mu \, \partial w / \partial r \, . \tag{43}$$

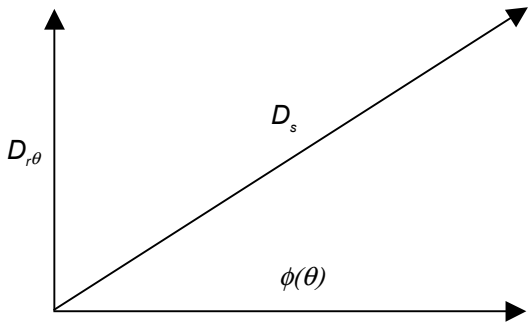

Figure 21. Shear stress plane defined by ϕ *on* r = a.

This stress is greatest on the rotor at $r = a$. It follows from this that we need to look for the principal axis and principal tensile stress of the stress deviator

$$\left[\mathbf{S}\right] = 2\mu \begin{bmatrix} 0 & D_{r\theta} & D_{rz} \\ D_{r\theta} & 0 & 0 \\ D_{rz} & 0 & 0 \end{bmatrix} \tag{44}$$

at $r = a$. This problem may be reduced to a two-dimensional one in a plane at an angle $\phi(\theta)$ from the z,r plane, as in figure 21. The shear strain in this plane is

$$D_{rs}(\theta) = \sqrt{D_{r\theta}^2(\theta) + D_{rz}^2(\theta)} \tag{45}$$

The principal direction for the opening is 45 deg. in the plane ϕ of D_{rs}.

Figure 20 compares the values of the principal stress with the pressure when there is axial flow when Ωa = 1600 cm/s and $\tilde{e} = 0.265$ (*c.f.* figure 19). The axial velocity increases with the axial pressure gradient; a pressure gradient of 41.4 kPa is typical for the EQM apparatus. The tensile stress increases with the axial flow because D_{rz} increases strongly.

11 Conclusions

The flow between eccentric cylinders with a constant axial pressure gradient was simulated successfully using the computational code SIMPLER.

The most dominant factor in the deformation of an emulsion is the pressure gradient between the maximum and minimum pressure near the minimum gap. The shear stress and extensional stress have a relatively small effect.

There is a large eddy at the top of the journal bearing; in order to mill an emulsion the inlet port has to be near the bottom where there is no eddy. Moreover, to obtain samples of this flow once it has been milled, the outlet port has to be located far from the eddy region.

The Reynolds number has a marked effect on the symmetry and magnitude of the high-low pressure region. At low Reynolds numbers the eddy is symmetric, but at high Reynolds numbers the eddy moves to one side in the direction of rotation. Moreover, the eddy gets larger as the eccentricity is increased.

The numerical results at low Reynolds numbers validate the lubrication approximations and at high Reynolds numbers they show a strong increase in the magnitude of the positive pressure and decrease in the magnitude of negative pressure.

The cavitation threshold in a journal bearing is lower when the criterion for cavitation is based on the maximum tensile stress rather than pressure. The maximum tensile stress is found no the rotor where the motion is purely shearing. The stress tensor there is diagonal at an angle 45 deg. from the direction of pure shear; at 45 deg. from the shearing plane.

Acknowledgement

This work was supported by the NSF under GOALI grant (Grant Opportunities for Academic Liaisons with Industry), by the Engineering Division of the Office of Basic Energy Sciences of the DOE and PDVSA INTEVEP S.A. Venezuela.

References

[1] Patankar S.V. (1980). *Numerical Heat Transfer and Fluid Flow*. Hemisphere, New York, USA, pp. 26, 30, 35, 118, 120, 147.

[2] Joseph, D.D., McGrath, G., Nuñez, G. and Ortega, P. (1999). Apparatus and method for determining dynamic stability of emulsions. US patent 5, 987,969, Nov 23.

[3] Joseph, D.D. (1998), Cavitation and the state of stress in a flowing liquid. *J. Fluid Mech*, **366**, 367-378.

[4] Wannier, G. (1950). A contribution to the hydrodynamics of lubrication, Quart. Appl. Math., 8, 1-32.

[5] Szeri A.Z., Al-Sharif A. (1995*)*. Flow Between Finite, Steadily Rotating Eccentric Cylinders, *Theoretical and Computational Fluid Dynamics*, 7 pp. 12.

List of Symbols

a	rotor radius length, cm.
$\tilde{a}$	rotor radius length, dimensionless.
b	stator radius length, cm.
$\tilde{b}$	stator radius length, dimensionless
c	clearance, cm.
$\tilde{c}$	clearance, dimensionless.
D	rate of stress tensor.
e	eccentricity, cm
$\tilde{e}$	eccentricity, dimensionless.
h	gap, cm.
h_m	film thickness, cm.
h_{max}	maximum thickness, cm.
h_{min}	minimum thickness, cm.
i	index for angular segments.
j	index for radial segments.
L	total angular segments.
M	total radial segments.
Q	orthogonal transformation tensor.
r	radial component/radial length, cm.
$\tilde{r}$	radial component/radial length, dimensionless.
u	angular velocity, cm/s.
$\tilde{u}$	angular velocity, dimensionless.
U	rotor velocity at r = a, cm/s
$\tilde{U}$	rotor velocity at r = a, dimensionless.
ν	radial velocity, cm/s.
$\tilde{v}$	radial velocity, dimensionless.
w	axial velocity, cm/s.
$\tilde{w}$	axial velocity, dimensionless.
z	axial component/axial length (cm).
p	pressure, Pa
$\tilde{p}$	pressure, dimensionless
$\bar{p}$	average pressure, Pa.
p_{abs}	absolute pressure, Pa
p_c	cavitation pressure, Pa
p_{max}	maximum pressure, Pa
p_{min}	minimum pressure, Pa
p_r	reference pressure, Pa
Re	Reynolds number, dimensionless.
S	deviator stress tensor.
T	stress tensor.
δ	minimum gap, cm.
ε	eccentricity ratio.
ϕ	angle on the *z,r* plane, deg.
$\tilde{\delta}$	minimum gap, dimensionless.
μ	dynamic viscosity, Pa·s
θ	angular component/angular length (deg.).
θ_m	angular position at max/min pressure, deg.
ρ	density, kg/m^3.
$\Re$	axial pressure gradient, kg/m^{2}s^2
$\tilde{\Re}$	axial pressure gradient, dimensionless.
Ω	angular velocity, rpm.
ψ	diagonalizing angle, deg.
ζ	special coordinate system.